ACS APPLIED MATERIALS & INTERFACES

Research Article

www.acsami.org

Thin Film Multiferroic Nanocomposites by Ion Implantation

Miguel Algueró,*[,†] Jesús Ricote,[†] María Torres,[†] Harvey Amorín,[†] Aurora Alberca,[†] Oscar Iglesias-Freire,[†] Norbert Nemes,[‡] Susana Holgado,[§] Manuel Cervera,[∥] Juan Piqueras,[∥] Agustina Asenjo,[†] and Mar García-Hernández[†]

[†]Instituto de Ciencia de Materiales de Madrid (ICMM), Consejo Superior de Investigaciones Científicas (CSIC), Cantoblanco, Madrid, 28049 Madrid, Spain

[‡]GFMC, Departamento de Física Aplicada III, Facultad de Física, Universidad Complutense de Madrid (UCM), Madrid, 28040 Madrid, Spain

[§]Departamento de Tecnología Electrónica y de las Comunicaciones, Escuela Politécnica Superior, Universidad Autónoma de Madrid (UAM), Madrid, 28049 Madrid, Spain

[∥]Laboratorio de Microelectrónica, Facultad de Ciencias, Universidad Autónoma de Madrid (UAM), Madrid, 28049 Madrid, Spain

Supporting Information

ABSTRACT: Thin film multiferroic nanocomposites might enable a range of potentially disruptive integrated magnetoelectric devices for information storage, spintronics, microwave telecommunications, and magnetic sensing. With this aim, we have investigated ion implantation of magnetic species into ferroelectric single crystal targets as a radically novel approach to prepare film nanoparticulate magnetic-metal ferroelectric-oxide composites. These materials are an alternative to multiferroic oxide epitaxial columnar nanostructures that are under intensive research, but whose magnetoelectric response is far from expectations. Here, we unambiguously demonstrate the preparation of such a thin film multiferroic nanocomposite of Co and $BaTiO_3$ by ion implantation of a high dose of the magnetic species, followed by rapid thermal processing under tailored conditions. Results thus constitute a proof of concept for the feasibility of obtaining the materials by this alternative approach. Ion implantation is a standard technique for the microelectronic industry in combination with well-established patterning procedures.

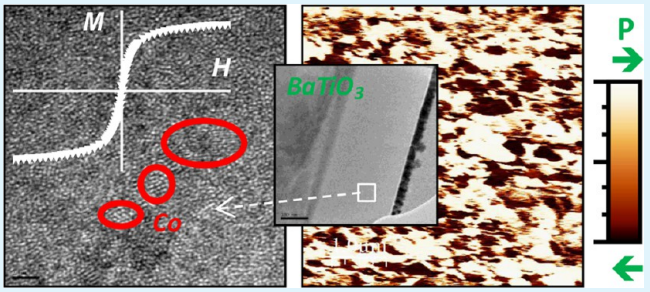

KEYWORDS: *ion-implantation, magnetoelectric-devices, multiferroic-materials, nanoparticulate-composite, thin-film-technologies*

INTRODUCTION

The solid state linear magnetoelectric effect is the generation of an electrical polarization proportional to an applied magnetic field (direct effect) and of a magnetization in response to an electric field (converse effect).[1] Research of single-phase materials has mainly concentrated on multiferroics,[2−4] because they are also liable to show magnetoelectric switching: the reversal of magnetization with the electric field. This might be the key to electrical-writing and magnetic-reading in random access memories.[5] The memory device is only an example of the range of potentially disruptive magnetoelectric technologies that have been proposed for information storage, spintronics, microwave signal processing, and magnetic field sensing.[6,7] However, and in spite of the intensive research,[8−10] a single-phase material multiferroic at room temperature and with significant magnetoelectric coupling has not been reported yet.

An alternative to single phase materials are two-phase ferromagnetic-ferroelectric composites.[11,12] In these materials, the magnetoelectric effect is obtained as a product property of the magnetostriction and piezoelectricity of the phases. The best results have been obtained with laminate composites of a high-permeability magnetostrictive FeBSiC alloy and ultrahigh piezoelectricity $Pb(Mg_{1/3}Nb_{2/3})O_3$−$PbTiO_3$ fibers with a 2−1 connectivity, which showed a magnetoelectric coefficient α_E > 50 V cm^{-1} Oe^{-1}. Magnetic field sensors with extremely low equivalent magnetic noise and sensitivity as high as 10 pT have been demonstrated with these laminates.[13]

The challenge now is to develop comparable materials in thin film form for integrated technologies.[14] Attention has mainly concentrated in epitaxial columnar nanostructures of magnetic spinel- and ferroelectric perovskite-structure oxides like $CoFe_2O_4$ and $BaTiO_3$ or $BiFeO_3$.[15−17] A 1−3 connectivity is engineered to avoid substrate clamping effects. Though magnetoelectric switching has been locally demonstrated and controlled,[18] an analogous macroscopic effect has not been obtained, and only very recently an unambiguous magnetoelectric response was reported, yet with low coefficients of 0.06 V cm^{-1} Oe^{-1}.[19]

Received: November 5, 2013
Accepted: January 13, 2014
Published: January 13, 2014

dx.doi.org/10.1021/am404945m | ACS Appl. Mater. Interfaces 2014, 6, 1909−1915

The substrate clamping issue can also be minimized by selecting 0−3 connectivity, and most promising results have been found for thin film particulate nanocomposites of Co and $BaTiO_3$ with magnetoelectric coefficients of 0.16 V cm^{-1} Oe^{-1}.[20] After this report, we have investigated the preparation of such film magnetic-metal ferroelectric-oxide composites by a radically novel approach: the ion implantation of magnetic species into ferroelectric single crystal targets. Indeed, we focused a first study on the Co implantation of $Pb(Mg_{1/3}Nb_{2/3})O_3$−$PbTiO_3$ single crystals and showed the formation of an ensemble of ferromagnetic nanoparticles embedded in an amorphized layer at the surface of the ferroelectric crystal.[21] Similar effects were described with $BaTiO_3$ targets in an independent research.[22] However, none of these studies addressed the recovery of the implantation damage and thus of the ferroelectricity of the surface layer. Therefore, an actual proof of concept was not provided. This is done here for the case of Co and $BaTiO_3$.

EXPERIMENTAL METHODS

Commercial, ⟨100⟩-oriented $BaTiO_3$ single crystal plates with 5 × 5 × 1 mm^3 dimensions were used as targets (MaTecK GmbH). Co+ implantation was carried out with the 200 keV-high current implanter at Forschungszentrum Dresden-Rossendorf (Germany) with a beam spot size of ∼15 nm and electrostatic scan. A high dose of 1 × 10^{17} Co ions cm^{-2} was implanted aiming at inducing clustering. Sample surface temperature was maintained below 200 °C during implantation. Simulation with SRIM-2008.04 resulted in a projected range of 92 nm and a longitudinal straggling of 42 nm with the 200 keV energy ions used. Details of this simulation procedure can be found elsewhere.[23] Input parameters are the ion species and energy and target composition and density.

The appearance of magnetism in the implanted crystals was followed with a superconducting quantum interference device (SQUID) magnetometer, by measuring magnetization as a function of magnetic field at room temperature. Also, its surface component was studied by magnetic force microscopy (MFM). A commercial SFM-MFM system from Nanotec Electrónica was used. Probes were commercial Nanosensors PPP-MFMR cantilevers with a force constant of 1.5 N/m and a resonance frequency of 75 kHz, which are magnetized along their pyramid axis before the experiment.

Changes in the crystal surface ferroelectricity after implantation were monitored by piezoresponse force microscopy (PFM). A second scanning force microscope was used (also from Nanotec Electrónica). In these measurements, AC voltages between 2 and 10 V_{pp} (peak-to-peak) at 50 kHz were applied between the tip and the sample to study the local piezoelectric response. Conductive commercial Pt/Ir coated tips (Nanosensors NCH-Pt) on cantilevers with force constants of 42 N/m and resonance frequencies of 320 kHz were chosen in this case.

Structural and compositional gradients in the implanted layers were characterized by high resolution transmission electron microscopy (HRTEM), high angle annular dark field scanning transmission electron microscopy (HAADF-STEM), and energy dispersive X-ray spectroscopy (EDXS). Measurements were accomplished with a Tecnai-20 FEG TEM working at 200 kV. A cross section sample was prepared by focused ion beam (FIB) patterning for these studies.

Spectroscopic ellipsometry was also used as an alternative, nondestructive method to investigate gradients across layers. A phase-modulated ellipsometer UVISEL (Horiba Ivon SAS) operating between 1.5 and 4.5 eV was used. Spectra were simulated with a four-/three-layer model (three/two films and substrate) of variable percentages of $BaTiO_3$, metallic Co, and voids by using the Bruggeman effective medium approximation.[24]

The recovery of the implantation damage was addressed by rapid thermal processing (RTP) in Ar. A heating rate of 10 °C s^{-1} and typical processing times of 30 min at increasing temperatures up to 700 °C (well above the Curie temperature of 120 °C) were used. The perovskite recrystallization process was followed with spectroscopic ellipsometry and confirmed with grazing incidence X-ray diffraction (GIXRD). A Siemens D500 powder diffractometer adapted to the asymmetric Bragg configuration, Cu K_α radiation, and an incident angle of 3° were used. Changes in magnetism and surface ferroelectricity after the RTP thermal treatments were characterized with the same, previously described techniques.

RESULTS AND DISCUSSION

Magnetism directly resulted from the implantation of a high dose of the magnetic species into the $BaTiO_3$ target, as shown by superconducting quantum interference device magnetometry. The room temperature magnetization loop of an implanted crystal is shown in Figure 1, which has a coercive

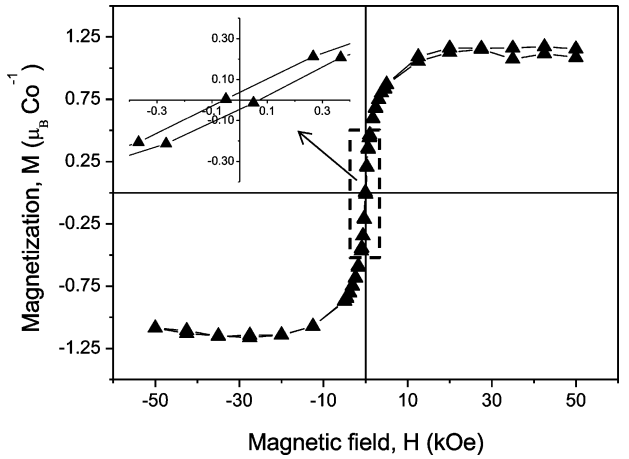

Figure 1. Room temperature magnetic response of a Co-implanted $BaTiO_3$ single crystal.

field of ≈65 Oe and saturation and remnant magnetizations of ≈1.05 and 0.04 μ_B Co^{-1}, respectively. It is remarkable the low remanence, indicating a quasi-superparamagnetic regime that suggests the very small size of the existing magnetic entities. Magnetic force microcopy was also carried out, but negligible surface magnetization near the noise range of the technique was found. This indicates magnetic species to be buried.

The location and nature of the magnetic entities was further investigated during the high resolution transmission electron microscopy and high angle annular dark field scanning transmission electron microscopy experiments, carried out on the cross section specimen. A general view is shown in Figure 2a. The bulk, nonmodified $BaTiO_3$ single crystal is at the left side of the image and will be referred from now on as substrate. The modified layer extends up to the very thin dark layer at the right side that is a protective Pt coating deposited to avoid damage during the FIB patterning. Therefore, a modified layer of about 260 nm resulted from the implantation. A HRTEM image across the boundary between the substrate and the modified layer is shown in Figure 2b, where an abrupt interruption of the crystal lattice fringes takes place (this is clearer in the additional images given in the Supporting Information). Note also the Fast Fourier Transform (FFT) analysis of the two areas given in the image. All this indicates the layer to be an amorphized one as a result of the implantation.

A HAADF-STEM image of the same cross section sample directly comparable to the bright field TEM of Figure 2a is given in Figure 3a. The absence of contrast between the

dx.doi.org/10.1021/am404945m | ACS Appl. Mater. Interfaces 2014, 6, 1909−1915

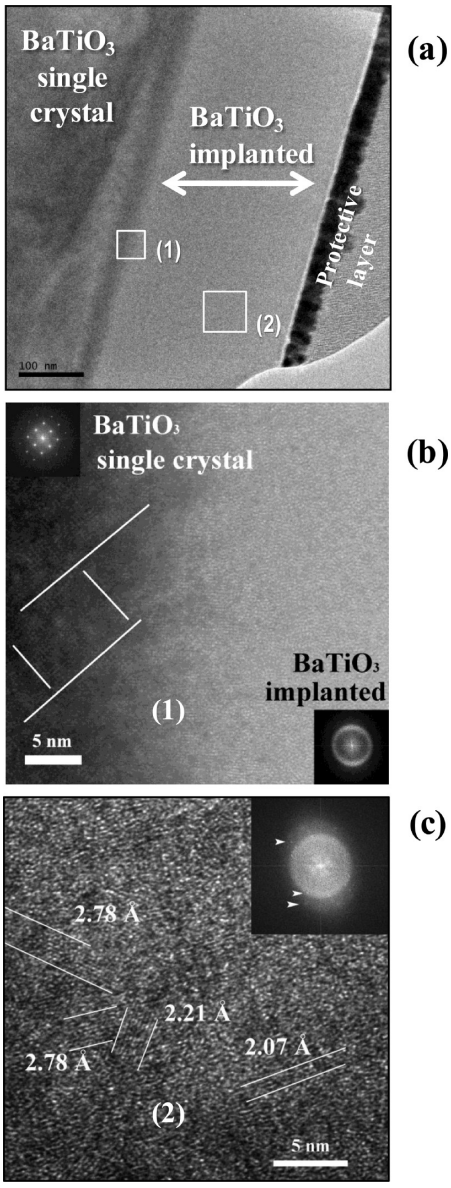

Figure 2. (a) TEM image of a Co-implanted $BaTiO_3$ crystal cross section. (b,c) HRTEM images and associated FFT analysis of the areas labeled with (1) and (2) in (a). Lines are a guide to the eye for lattice fringes.

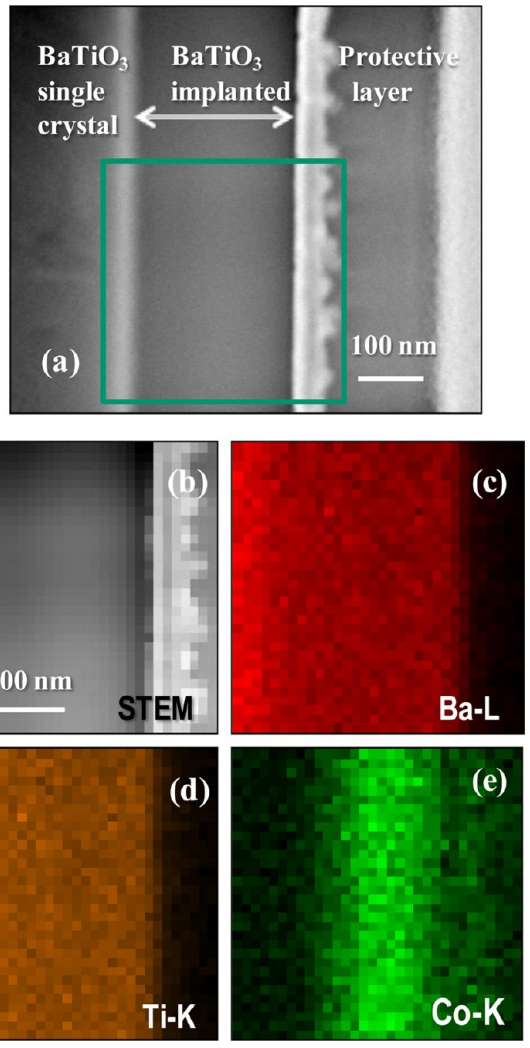

Figure 3. (a) HAADF-STEM image of the same area of Figure 2a, (b) STEM image of the area selected for EDXS studies, and (c–e) corresponding Ba, Ti, and Co EDXS signal mappings.

substrate and the amorphized layer indicates the average atomic number to be basically the same in the two areas. Expected compositional differences, mainly Co gradients, were further investigated by EDXS. Some selected mappings corresponding to the area shown in Figure 3b are given in Figures 3c–e, where the distribution of Co is compared with that of Ba and Ti. Note that cobalt is mostly localized in a layer of 160 nm thickness with a maximum concentration at the subsurface (100 nm from the surface). This value compares well with the projected range of 92 nm anticipated by the simulation with SRIM. However, the thickness of the Co-rich layer is significantly larger than that expected from the longitudinal straggling: 42 nm obtained by simulation for the implantation conditions used. Also, note also that the amorphous layer extends much deeper into the crystal than the Co signal does in the EDXS mapping. The end of range damaged region beyond the projected penetration is usually observed for large implanted doses.[25] We will come back to this point later on.

Additional HRTEM experiments were focused on the Co rich layer and showed the presence of nanoparticles with size of a few nm at the subsurface, as it is illustrated in Figure 2c. A range of lattice fringe spacings were measured (~2.07, 2.21, 2.78 Å, ...), which do not correspond to those of $BaTiO_3$ (see JCPDS-ICDD-PDF 5-626 and 31-174 for the tetragonal and cubic polymorphs, respectively), and could not be associated with a single phase. Coexistence of metallic Co nanoparticles with a range of oxide ones is suggested, for small spacings are compatible with metallic Co (see JCPDS-ICDD-PDF 5-727 for the hexagonal phase with 2.023 and 2.165 Å for 002 and 100 planar distances, respectively, or PDF 15-806 for the cubic phase with 2.0467 Å for 111 distance), while larger spacings are not and are likely associated with cobalt oxides (see JCPDS-ICDD-PDF 2-770 for Co_2O_3 with 2.87 Å for 002 planar distance, PDF 42-1467 for Co_3O_4 with 2.858 Å for 220 distance, and PDF 42-1300 for CoO with 2.6235 Å for 111) .

The phenomenology described up to now is very similar to that previously reported for the Co implantation of $Pb(Mg_{1/3}Nb_{2/3})O_3–PbTiO_3$.[21] Therefore, one can analogously conclude that $BaTiO_3$ perovskite amorphization readily takes

dx.doi.org/10.1021/am404945m | ACS Appl. Mater. Interfaces 2014, 6, 1909–1915

place at the early stages of implantation, for relatively low Co levels. Dynamical heating most probably also occurs during the process,[25] which would be responsible for the experimental Co longitudinal straggling being significantly larger than simulated, and of the amorphization edge that extends far beyond the Co end. However, unlike the case of $Pb(Mg_{1/3}Nb_{2/3})O_3-PbTiO_3$, large oxide particles do not appear in the Co-rich area as an implantation chemical effect. In this case, an ensemble of coexisting, very small metallic Co and oxide particles is formed. Formation of an ensemble of Co nanoparticles was hypothesized in the only one previous work based on the magnetic properties.[26]

A straightforward consequence of the layer amorphization must be the disappearance of ferroelectric long-range order. Ferroelectricity is a well-known cooperative phenomenon among individual dipolar moments intrinsically linked to the crystal structure and specifically to the tetragonal distortion in the case of $BaTiO_3$. Size decrease or extensive defects as those introduced during implantation reduce the coherence length of the distortions and thus can result in a vanishing of ferroelectricity.[27] We will show later this to be the case.

Amorphization also has direct implications in the objective of the research. At this stage, one cannot say that a multiferroic film composite has been obtained, for the implantation damage would have destroyed ferroelectricity at the surface layer. Therefore, it was necessary to address the recrystallization of the perovskite.

This was done by rapid thermal processing (RTP). Experiments involved a number of cumulative thermal treatments at increasing temperatures, after which one preparation of cross section specimens for TEM was not feasible. Therefore, spectroscopic ellipsometry was used as an alternative, nondestructive method to follow the recrystallization process.

The optical pseudodielectric constant of the implanted crystal is shown in Figure 4 before and after full recrystallization. Results for the implanted crystal reflected the severe damage caused by the ion beam. We tried to fit the experimental results to the four-layer structure suggested by TEM measurements, a surface layer of crystalline $BaTiO_3$ plus voids (usually introduced to account for surface roughness) of about 20 nm, an implanted subsurface layer of 160 nm of $BaTiO_3$ plus Co, an underneath layer of 80 nm of $BaTiO_3$ plus voids (to account this time for the end of range damaged region), and the $BaTiO_3$ substrate. Using the dielectric constant of crystalline $BaTiO_3$,[28] no reasonable fittings were obtained. As an example, the simulated pseudodielectric constant for a surface layer with a 0.18 fraction of voids, an implanted subsurface layer with 0.08 Co fraction and a nearly transparent underneath layer (0.83 fraction of voids), the structure that provided the "best" fit, is included in the figure. Indeed, not only agreement is very poor (and releasing thickness did not improve it), but results are also unphysical because a void fraction of 0.83 cannot be rationalized. All this is most probably a consequence of the dielectric constant of amorphous $BaTiO_3$ being far from the crystalline one[29] and also of the extensive bond breakdowns, oxygen losses, and partial Co oxidation that take place under the implantation conditions used (1×10^{17} Co^+ cm^{-2} dose, 200 keV energy). Basically, these results indicate the strong modification of the optical polarizability of $BaTiO_3$ after its amorphization during implantation.

The situation was completely different for the implanted crystal thermally treated at 700 °C. Agreement between

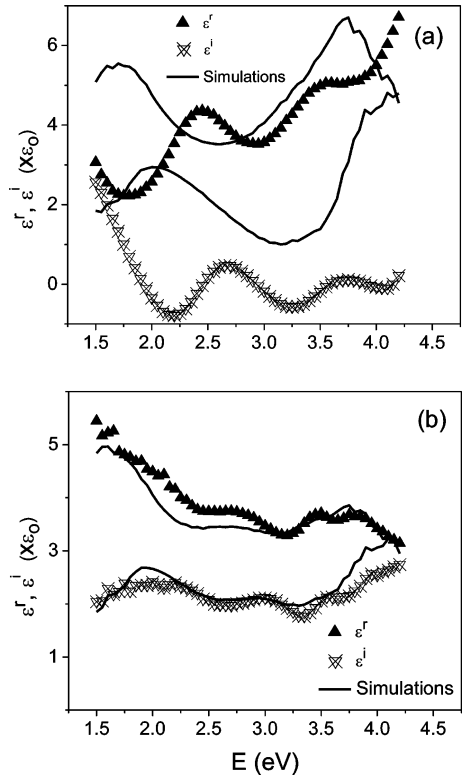

Figure 4. Ellipsometric spectrum (real and imaginary pseudodielectric permittivity, ε^r and ε^i) of a Co-implanted $BaTiO_3$ (BTO) crystal (a) before and (b) after rapid thermal processing (RTP), and best simulations with (a) four-/(b) three-layer model (Before RTP; 1-(20 nm): 0.82 BTO + 0.18 voids, 2-(160 nm) 0.92 BTO + 0.08 Co, 3-(80 nm): 0.17 BTO + 0.83 voids, 4: BTO. After RTP; 1-(27 nm): 0.66 BTO + 0.34 voids, 2-(187 nm) 0.97 BTO + 0.03 Co, 3: BTO).

experimental data and the best fit with the same previous four-layer model was remarkable. Moreover, parameter (thickness and phase fractions) optimization indicated the full recovery of the underneath damaged layer (no voids). Experimental and simulated spectra for the recrystallized sample are shown in Figure 4b. The best results were obtained for a surface layer of 27 nm with a void fraction of 0.34 (that in this case can be associated with surface roughness) and a subsurface implanted layer of 187 nm with a 0.03 fraction of Co (indicating gradient to smear out during the RTP treatment).

Perovskite structure recrystallization was confirmed with grazing incidence X-ray diffraction (GIXRD), and results are summarized in Figure 5. No diffraction peaks appeared in the GIXRD pattern of the $BaTiO_3$ single crystal before implantation (the Bragg condition is not fulfilled by the (001) planes of the crystal surface in this geometry) nor in the pattern of the crystal implanted with the high dose of Co. In contrast, a set of diffraction peaks appears in the implanted crystal after rapid thermal processing at 700 °C in Ar. A very good agreement is found between peaks and the lines corresponding to polycrystalline $BaTiO_3$ (JCPDS-ICDD-PDF 4-0686, see Figure 5b), so perovskite recrystallization did take place by RTP.

The layer perovskite recrystallization anticipated the recovery of the surface ferroelectricity as corroborated by piezoresponse force microscopy. Piezoresponse amplitude and phase images of the implanted crystal surface before and after rapid thermal processing are shown in Figure 6. Comparable images for a

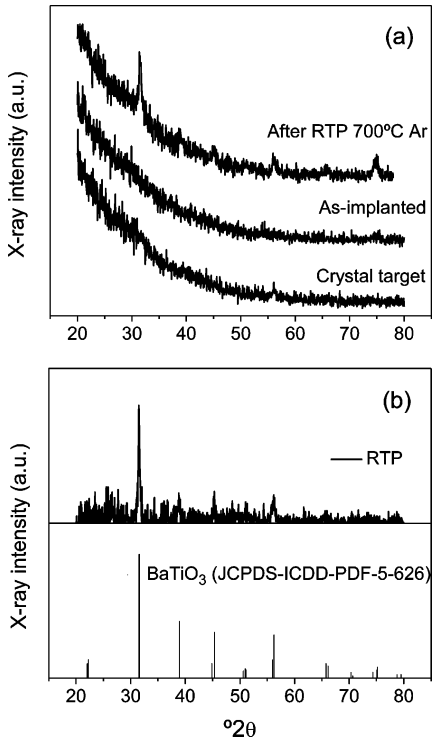

Figure 5. (a) GIXRD patterns of the implanted crystal before and after RTP and (b) identification of the crystalline phase as polycrystalline $BaTiO_3$ (JCPDS-ICDD-PDF 4-0686).

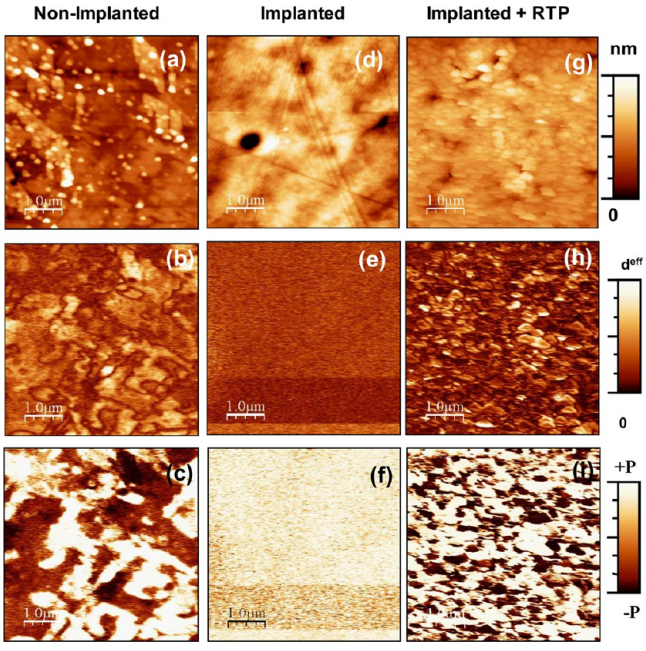

Figure 6. Topographic (a,d,g), and piezoresponse amplitude (b,e,h) and phase (c,f,i) images of a $BaTiO_3$ single crystal surface before (a–c) and after (d–f) implantation and after RTP (g–i). (b,c,e,f) are out-of-plane piezoresponse images, while (h,f) are in-plane ones.

single crystal target before implantation are also included, along with all topographic images. Crystals were implanted as-received, and mirror-polished surfaces showed a topography with terraces along with polishing defects (see Figure 6a) that was flattened out during implantation (Figure 6d). As-received crystals showed the standard ferroelectric domain hierarchical configuration of 90° and 180° domains,[30] as revealed by the PFM studies (additional piezoresponse images are given in the Supporting Information). No piezoresponse signal was found in the implanted layer (see Figures 6e and f), which indicated the disappearance of ferroelectricity as a result of the implantation damage as previously discussed.

Topography evolved during recrystallization (see Figure 6g), reflecting the development of a fine grained microstructure, in agreement with the polycrystalline character of the recrystallized layer indicated by the GIXRD results. Piezoresponse was recovered after RTP as clearly shown by the amplitude and phase images of Figures 6h and i. Note also the direct correlation between microstructure and domain configuration, which indicates single domain grains, in agreement with previous reports for nanostructured $BaTiO_3$.[31]

Results clearly indicated the presence of an out-of plane self-polarization in the recrystallized film. This is illustrated in Figure 7, where out-of-plane and in-plane piezoresponse images

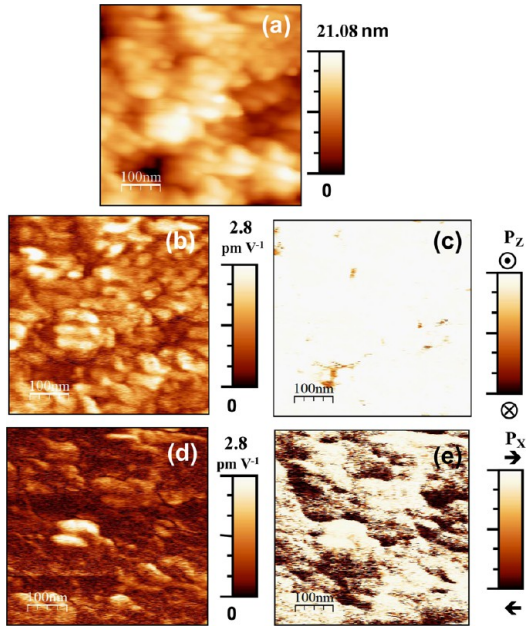

Figure 7. High magnification (a) topographic, (b,c) out-of-plane piezoresponse (amplitude, phase), and (d,e) in-plane piezoresponse (amplitude, phase) images of a $BaTiO_3$ surface after implantation and RTP.

for a reduced area are shown together. An internal electric field thus seemed to exist across the layer. Its origin is out of the scope of this work but might be caused by a strain gradient through the flexoelectric effect. It is worth noting that self-poling could be advantageous for the potential magnetoelectric functionality of the material.[32]

The last key aspect is the maintenance of the ferromagnetism after the RTP thermal treatment. Indeed, the disappearance of the ferromagnetism was previously reported after thermal treatment in air of Co implanted $BaTiO_3$ layers.[22] However, the use of RTP and an Ar atmosphere allow preserving magnetism, as shown in Figure 8. The main effects are a moderate decrease of the saturation magnetization, from ≈1.05 down to 0.85 μ_B Co^{-1}, and a slight increase of the remanence, from 0.04 up to 0.06 μ_B Co^{-1}, and of the coercive field, up to ≈80 Oe. No contrast appeared in the MFM images, as expected from the decrease of magnetization.

dx.doi.org/10.1021/am404945m | ACS Appl. Mater. Interfaces 2014, 6, 1909–1915

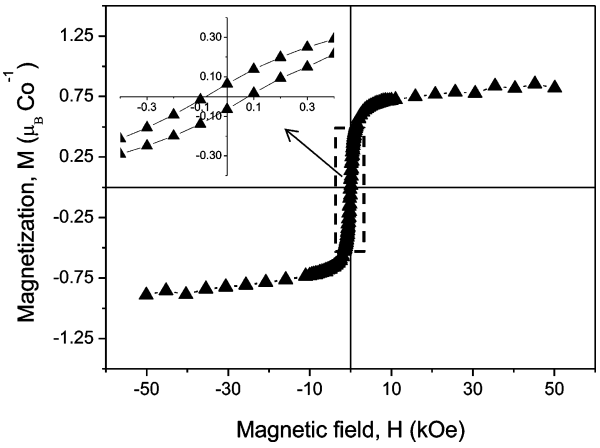

Figure 8. Room temperature magnetic response of a Co-implanted $BaTiO_3$ single crystal after RTP.

On one hand, these changes in magnetism after RTP can be understood as a consequence of a limited, partial oxidation of the metallic Co nanoclusters. This would explain the decrease in saturation magnetization, and also the increase in coercive field, this as a consequence of oxygen diffusion into the metallic particles, and the formation of an interpenetrating metal oxide micro(nano)-structure. This process would occur in spite of the Ar atmosphere because of the high oxygen content of the amorphous matrix surrounding the particles. An alternative mechanism could be the dissolution of the smallest metallic clusters into the perovskite structure, though titania nanocrystals should then appear. On the other hand, the slight increase of remanence indicates an improvement of the crystallinity of the remaining Co clusters.

Functional characterization was attempted, for which Au/Pt interdigital electrodes (IDEs) were deposited by sputtering and a lift-off process. Complex impedance measurements indicated high conductivity (room temperature parallel resistance of ~1 kΩ already at 1 MHz), which prevented polarization measurements. The surface is free of metallic cobalt clusters, so charge carriers must be associated with the recrystallized-perovskite defect chemistry. This should be liable of tailoring by varying the Co dose and the RTP parameters. Indeed, preliminary results have shown that decreasing the Co dose down to 2×10^{16} Cm^{-2} allows an insulating perovskite to be obtained after the same RTP, while maintaining a saturation magnetization of 0.90 μ_B Co^{-1}. Also, electrical tuning of the ferromagnetic resonance has been reported for Co-implanted $BaTiO_3$ before recrystallization.[26,33] This magnetoelectric effect demonstrates the elastic coupling between the Co clusters and amorphized perovskite.

SUMMARY AND CONCLUSIONS

We have shown that ion implantation of a high dose of magnetic Co into ferroelectric $BaTiO_3$ crystals resulted in cobalt nanoclusters, directly observed by HRTEM, embedded in an amorphized oxide matrix at the subsurface. Rapid thermal processing in Ar allowed the perovskite recrystallization and, so, the recovery of ferroelectricity while maintaining the ferromagnetism of the Co nanoparticles. These results unambiguously demonstrate the preparation of a thin film multiferroic nanoparticulate composite of Co and $BaTiO_3$ by this procedure. They thus constitute a proof of concept for the feasibility of obtaining these key materials by the alternative novel approach. Ion implantation is a standard technique for the microelectronic industry routinely used in combination with well-established patterning procedures. The next step must be the implantation of epitaxial films, ideally on conductive substrates, which would also facilitate functional characterization. These film composite materials might enable a range of integrated magnetoelectric technologies like memories, spintronic devices, tunable microwave components, and magnetic field sensors.

ASSOCIATED CONTENT

Supporting Information

Sequence of HRTEM images across the boundary between the underlying nonmodified target and the modified layer by implantation; PFM images of the initial ferroelectric domains in the $BaTiO_3$ targets. This material is available free of charge via the Internet at http://pubs.acs.org.

AUTHOR INFORMATION

Corresponding Author

*E-mail: malguero@icmm.csic.es.

Notes

The authors declare no competing financial interest.

ACKNOWLEDGMENTS

Funded by MINECO (formerly MICINN, Spain) through projects MAT2011-23709 and MAT2009-07551-E. Implantations were carried out within the TNA Programme of the European Commission Integrated Infrastructure Initiative (I3) SPIRIT (Support of Public and Industrial Research Using Ion Beam Technology) under EC contract no. 227012.

REFERENCES

(1) Fiebig, M. *J. Phys. D: Appl. Phys.* **2005**, *38*, R123−R152.
(2) Eerenstein, W.; Mathur, N. D.; Scott, J. F. *Nature* **2006**, *442*, 759−765.
(3) Cheong, S. W.; Mostovoy, M. *Nat. Mater.* **2007**, *6*, 13−20.
(4) Ramesh, R.; Spaldin, N. A. *Nat. Mater.* **2007**, *6*, 21−29.
(5) Bibes, M.; Barthelemy, A. *Nat. Mater.* **2008**, *7*, 425−426.
(6) Bea, H.; Gajek, M.; Bibes, M.; Barthelemy, A. *J. Phys.: Condens. Matter* **2008**, *20*, 434221.
(7) Scott, J. F. *J. Mater. Chem.* **2012**, *22*, 4567−4574.
(8) Catalan, G.; Scott, J. F. *Adv. Mater.* **2009**, *21*, 2463−2485.
(9) Tokura, Y.; Seki, S. *Adv. Mater.* **2010**, *22*, 1554−1565.
(10) Castro, A.; Correas, C.; Peña, O.; Landa-Canovas, A. R.; Alguero, M.; Amorin, H.; Dolle, M.; Vila, E.; Hungria, T. *J. Mater. Chem.* **2012**, *22*, 9928−9938.
(11) Nan, C. W.; Bichurin, M. I.; Dong, S.; Viehland, D.; Srinivasan, G. *J. Appl. Phys.* **2008**, *103*, 031101.
(12) Vaz, C. A. F.; Hoffman, J.; Ahn, C. H.; Ramesh, R. *Adv. Mater.* **2010**, *22*, 2900−2918.
(13) Wang, Y.; Gray, D.; Berry, D.; Gao, J.; Li, M.; Li, J.; Viehland, D. *Adv. Mater.* **2011**, *23*, 4111−4114.
(14) Ma, J.; Hu, J.; Li, Z.; Nan, C. W. *Adv. Mater.* **2011**, *23*, 1062−1087.
(15) Zheng, H.; Wang, J.; Lofland, S. E.; Ma, Z.; Mohaddes-Aradabili, L.; Zhao, T.; Salamanca-Riba, L.; Shinde, S. R.; Ogale, S. B.; Bai, F.; Viehland, D.; Jia, Y.; Schlom, D. G.; Wuttig, M.; Roytburd, A.; Ramesh, R. *Science* **2004**, *303*, 661−663.
(16) Comes, R.; Liu, H.; Kholkhov, M.; Kasica, R.; Lu, J.; Wolf, S. A. *Nano Lett.* **2012**, *12*, 2367−2373.
(17) Liu, X.; Kim, Y.; Goetze, S.; Li, X.; Dong, S.; Werner, P.; Alexe, M.; Hesse, D. *Nano Lett.* **2012**, *11*, 3202−3206.

(18) Zavaliche, Z.; Zheng, H.; Mohaddes-Aradabili, L.; Yang, S. Y.; Zhang, Q.; Shafer, P.; Reilly, E.; Chopdekar, R.; Jia, Y.; Wright, P.; Schlom, D. G.; Suzuki, Y.; Ramesh, R. *Nano Lett.* **2005**, *5*, 1793−1796.
(19) Oh, Y. S.; Crane, S.; Zheng, H.; Chu, Y. H.; Ramesh, R.; Kim, K. H. *Appl. Phys. Lett.* **2010**, *97*, 052902.
(20) Park, J. H.; Jang, H. M.; Kim, H. S.; Park, C. G.; Lee, S. G. *Appl. Phys. Lett.* **2008**, *92*, 062908.
(21) Torres, M.; Ricote, J.; Amorin, H.; Jaafar, M.; Holgado, S.; Piqueras, J.; Asenjo, A.; García-Hernández, M.; Alguero, M. *J. Phys. D: Appl. Phys.* **2011**, *44*, 495306.
(22) Khalitov, N. I.; Khaibullin, R. I.; Valeev, V. F.; Dulov, E. N.; Ivoilov, N. G.; Tagirov, L. R.; Kazan, S.; Sale, A. G.; Mikailzade, F. A. *Nucl. Instrum. Methods Phys. Res., Sect. B* **2012**, *272*, 104−107.
(23) Ziegler, J. F.; Biersack, J. P.; Littmark, U. *The stopping and range of ions in solids*; Pergamon Press: New York, 1985 (SRIM-2008.04 software available at http://www.srim.org/).
(24) Tompkins, H. G. *A User's Guide to Ellipsometry*; Academic Press: New York, 1993; p 246.
(25) Krasheninnkov, A. V.; Nordlund, K. *J. Appl. Phys.* **2010**, *107*, 071301.
(26) Kazan, S.; Mikailzade, F. A.; Sale, A. G.; Maksutoglu, M.; Acikgoz, M. *Phys. Rev. B* **2010**, *82*, 054402.
(27) Smith, M. B.; Page, K.; Siegrist, T.; Redmond, P. L.; Walter, E. C.; Seshadri, R.; Brus, L. E.; Steigerwald, M. L. *J. Am. Chem. Soc.* **2008**, *130*, 6955−6963.
(28) Jellison, G. E., Jr.; Boatner, L. A.; Lowndes, D. H.; McKee, R. A.; Godbole, M. *Appl. Opt.* **1994**, *33*, 6053−6058.
(29) Lyahovitskaya, V.; Feldman, Y.; Zon, I.; Wachtel, E.; Gartsman, K.; Tagantsev, A. K.; Lubomirsky, I. *Phys. Rev. B* **2005**, *71*, 094205.
(30) Kalinin, S. V.; Bonnell, D. A. In *Nanoscale Characterization of Ferroelectric Materials*; Alexe, M., Gruverman, A., Eds.; Springer-Verlag: Berlin, 2004; p 1.
(31) Buscaglia, M. T.; Viviani, M.; Buscaglia, V.; Mitoseriu, L.; Testino, A.; Nanni, P.; Zhao, Z.; Nygren, M.; Harneaga, C.; Piazza, D.; Galassi, C. *Phys. Rev. B* **2006**, *73*, 064114.
(32) Zubko, P.; Catalan, G.; Tagantsev, A. K. *Annu. Rev. Mater. Res.* **2013**, *43*, 387−421.
(33) Khalitov, N. I.; Lyadov, N. M.; Valeev, V. F.; Khaibullin, R. I.; Faizrakhmanov, I. A.; Dulov, E. N.; Tagirov, L. R.; Ibragimov, S. Z.; Prikhodko, K. E.; Roddatis, V. V.; Maksutoglu, M.; Kazan, S.; Mikailzade, F. A. *Phys. Solid State* **2013**, *55*, 1279−1288.